Proceedings of CONF-CIAP 2026 Symposium: International Conference on Atomic Magnetometer and Applications
DOI: 10.54254/2753-8818/2026.HZ28741

Dynamic Evolution of Reionization Bubbles: Insights from THESAN Simulations

Chenyu Wang

The Independent School of Academy, HongKong, China
4024001@student.isf.edu.hk

Abstract. The Epoch of Reionization (EoR, z ≈ 6–20) marks the cosmic transition from a neutral to ionized intergalactic medium (IGM), driven by radiation from the first galaxies. This study synthesizes insights from two pivotal THESAN simulation papers to elucidate the dynamic evolution of ionized bubbles during reionization. A fundamental THESAN paper "The THESAN Project: properties of the intergalactic medium and its connection to reionization-era galaxies" establishes a framework linking IGM properties to reionization-era galaxies, revealing a late reionization history (z ≈ 5.5) consistent with Lyα forest observations and CMB optical depth constraints. "Connecting ionized bubble sizes to their local environments during the Epoch of Reionization" investigates the environmental dependence of bubble growth, identifying bimodal expansion: slow radiation-limited growth in early-reionized regions (z ≥ 10) versus rapid percolation and "flash ionization" in late-reionized voids (z ≤ 6). Our comparative analysis demonstrates that bubble growth follows three distinct phases: (1) isolated growth (xHI = 0.7); (2) percolation (0.3 < xHI < 0.7), driven by topological connectivity; and (3) runaway merging (xHI < 0.3), with front velocities >100 km s-1. Environmental overdensity (δ) critically modulates growth, with overdense regions hosting larger bubbles early on, while underdense voids exhibit delayed but explosive expansion. This paper introduce a unified growth model unifying both papers' insights, validated against THESAN data and JWST observations.This work reveals reionization's topology as a product of radiation physics, environmental feedback, and cosmic structure, advancing predictions for 21 cm and Lyα surveys.

Keywords: Reionization, ionized bubbles, THESAN simulations, galaxy formation

1. Introduction

The Epoch of Reionization (EoR), spanning approximately 200 < z < 6, represents one of the most transformative periods in cosmic history [1, 2]. During this era, ultraviolet radiation from the first galaxies and quasars ionized the neutral hydrogen that had pervaded the intergalactic medium (IGM) since recombination. This phase transition fundamentally altered the thermal and ionization state of the cosmos, setting the stage for galaxy formation as this paper observes it today. The spatial pattern of this transition—manifested as ionized "bubbles" expanding around luminous sources—encodes critical information about the nature of the first galaxies, the properties of dark matter, and the largescale structure of the universe. The THESAN simulation suite represents a quantum leap in

© 2025 The Authors. This is an open access article distributed under the terms of the Creative Commons Attribution License 4.0 (https://creativecommons.org/licenses/by/4.0/).

DOI: 10.54254/2753-8818/2026.HZ28741

modelling this epoch through its innovative coupling of radiation-hydrodynamics with realistic galaxy formation physics. This research synthesis focuses on two cornerstone papers from the collaboration. While THESAN simulation establishes the framework for connecting IGM properties to reionization-era galaxies, further study provides unprecedented insights into the environmental dependence of ionized bubble growth. Together, they reveal a complex tapestry of reionization patterns governed by the interplay between source properties, large-scale structure, and radiation transport physics. The paper is organized as follows. In Section 2, this papers summarize the two papers “The THESAN Project: properties of the intergalactic medium and its connection to reionization-era galaxies” and “Connecting ionized bubble sizes to their local environments during the Epoch of Reionization”, providing the scientific details of the different models. In Section 3 compares and contrasts the two papers, mainly pertaining to the research of the reionization bubble and BSD (bubble size distribution). In Section will present our research inferences about the pattern and the properties of the reionization bubbles based on our research on the two papers.

2. Current disvovery

2.1. The THESAN project: properties of the intergalactic medium and its connection to reionization-era galaxies

2.1.1. THESAN simulation

The paper introduces the THESAN simulation suite, a novel framework coupling radiation-magneto-hydrodynamics with the IllustrisTNG galaxy formation model to self-consistently simulate the Epoch of Reionization (EoR) and high-redshift galaxy evolution. It bridges cosmological-scale reionization and galaxy-scale physics by integrating radiative transfer (RT) with the calibrated IllustrisTNG galaxy model within a 95.5 cMpc volume, resolving haloes down to atomic cooling limits ($M_{halo} \sim 10^8 h^{-1} M\odot$).

2.1.2. Methodology

THESAN utilizes the moving-mesh code AREPO to solve radiation-magneto-hydrodynamics and gravity. Key innovations include self-consistent radiative transfer (RT) via AREPO-RT, discretizing UV photons into three bands (13.6–24.6 eV, 24.6– 54.4 eV, > 54.4 eV) using the M1 closure relation. Stellar spectra derive from BPASS v2.2.1 [2], while quasar spectra follow [3]. A reduced speed of light (c = 0.2c) is employed, resulting in less disturbance to the simulation result. Additionally, non-equilibrium solver for H/He ionization states and temperature, coupled with IllustrisTNG subgrid physics (e.g., star formation via effective EOS, black hole feedback). Dust evolution follows [4, 5]. The simulation was designed based on Planck Cosmology [4]. Flagship run (THESAN-1) has 2×2100^3 particles, gas mass resolution $m_{gas} = 5.82\times10^5 M_\odot$, and force softening of 2.2 ckpc. Medium-resolution variants (e.g., THESAN-2) explore escape fraction (f_{esc}) dependencies and dark matter models (e.g., sDAO). Forward modeling generates mock spectra using the Cosmic Lyα Transfer (COLT) code, ray-traced through the Voronoi mesh. Spectra include Voigt profile convolution, instrumental noise, and resolution degradation to match specific datasets.

2.1.3. Key result

THESAN produces a "late" reionization history ($z \sim 5.5$), consistent with Lyα emitter evolution, dark-pixel statistics, and CMB optical depth ($\tau_{CMB} = 0.057 \pm 0.007$). The mean free path ($\lambda_{mfp}$) grows

DOI: 10.54254/2753-8818/2026.HZ28741

rapidly from z = 6 to z = 5, matching recent observations (Becker et al. 2021), where λ_{mfp} is defined by the physical condition for Lyman-limit absorption: $\int_0^{\lambda} mfp\, ds\, \sigma_{912} n_{HI} = 1$. In this equation,$\sigma_{912}$ denotes the hydrogen ionization crosssection at 912Å, and n_{01} is the neutral hydrogen density. The extended photon propagation distances during late reionization directly manifest in the inhomogeneous temperature-density distributions of the post-reionization IGM (z < 6). Effective optical depth ($\tau_{eff} \equiv -ln\langle F \rangle$) distributions align with observations at z∼5.5 [6, 7]. Notably, THESAN is the first simulation to reproduce the observed modulation of Lyα flux with galaxy distance, signaling localized ionization bubbles. Responding to source sensitivity, dark-gap lengths (L_{dg}) and transmission-peak widths (w_p) correlate with source halo mass. Forcing only low-mass haloes ($M_{halo} < 10^{10}\ M_{\odot}$) to drive reionization suppresses intermediate-scale flux enhancement.

2.2. Connecting ionized bubble sizes to their local environments during the epoch of reionization

2.2.1. Background information

The paper mainly utilizes the THESAN and other simulations to reveal that ionized bubbles during the Epoch of Reionization grow through the distinct modes. The Epoch of Reionization (EoR; z ≈ 5−20) marks the transition from a neutral to an ionized intergalactic medium (IGM), driven by radiation from the first galaxies. Ionized bubbles surrounding luminous sources exhibit complex growth dynamics, with sizes constrained by Lyman-α damping wings (JWST) and 21-cm tomography (HERA / SKA). The THESAN radiation-hydrodynamic simulations model this process self-consistently, coupling IllustrisTNG galaxy formation with AREPO-RT radiative transfer in a L_{box} = 95.5 cMpc volume. Bubble sizes (Reff) are computed using the Mean-Free Path (MFP) method: $R_{eff} = \frac{1}{N_{rays}} \sum ri\,(i = 1), N_{rays} = 192$ where rays are traced from ionized cells (xHII ≥ 0.5) until intersecting neutral gas (x_{HI} < 0.5). Simulations resolve halos down to $M_{halo} \sim 10^8 h^{-1} M\odot$, with radiation transport solved via the M1 closure scheme.

2.2.2. Kernel discoveries

Bubble growth follows two distinct modes: The first mode is Early-reionized regions ($z_{reion} \geq 10$), which is a slow exponential growth (R_{eff} doubling time τ∼100Myr). The second mode is Late-reionized regions ($z_{reion} \leq 6$): "Flash ionization" into preexisting bubbles (R_{eff} ∼ 50cMpc), with ionization front velocities >104km/s. Size distributions transition from unimodal small bubbles (R_{eff}∼ 0.3cMpc at x_{HI}= 0.9) to percolated structures (R_{eff} > 50cMpc at x_{HI} = 0).

One main Environmental Dependence is overdensity, which is defined as $\delta \equiv (\rho - \rho^{-}) / \rho^{-}$. The overdensity correlates with bubble sizes. At x_{HI} > 0.5, bubbles in overdense regions $(log\,(1+\delta) > 0.5)$ are ∼20% larger than the global median. Power-law scaling $R_{eff} \propto M_{halo}$ flattens from α ≈ 0.29 (early EoR) to α ≈ 0.01 (late EoR). Bright galaxies (MUV < −20) reside preferentially in large bubbles, explaining JWST observational biases.

Also, the Redshift of Reionization is an effective parameter to probe the reionization bubbles. The redshift zreion (when xHII ≥ 0.5) traces small bubbles ($R_{eff} \leq$ 1cMpc) with minimal time delay. For R_{eff} >10cMpc, growth lags (Δt∼50Myr) weaken the correlation.

Overall, based on the comprehensive stimulation and analysis, the paper mainly draw 4 conclusions and enlightenments: (a). Bubble growth is bimodal: slow expansion in early-reionized regions vs. rapid percolation in late-reionized zones. (b). Overdense regions and massive galaxies

DOI: 10.54254/2753-8818/2026.HZ28741

host larger bubbles, but correlations weaken post-percolation. (c). JWST constraints (e.g., Hsiao et al. 2023) align with THESAN at $z \geq 9$, but tension emerges at $z \approx 7$ due to homogeneous IGM assumptions in idealized models.

(d). zreion is a robust probe for small-scale bubbles ($R_{eff} \leq$ 1cMpc) but unreliable for larger scales.

The paper well depicts the changing pattern and the properties of the reionization bubbles, providing reference value.

3. Contrast and comparison

The THESAN simulation suite ([1]; Kannan et al. 2022; Smith et al. 2022) represents a state-of-the-art framework for studying reionization through self-consistent radiation-magnetohydrodynamic simulations. This section provides a comprehensive comparison between two foundational THESAN papers. Both papers leverage THESAN's unique combination of the following four aspects: Large simulation volume (L_{box}= 95.5 cMpc); Highresolution galaxy formation model (IllustrisTNG physics); Selfconsistent radiative transfer (AREPO-RT); Non-equilibrium thermochemistry.

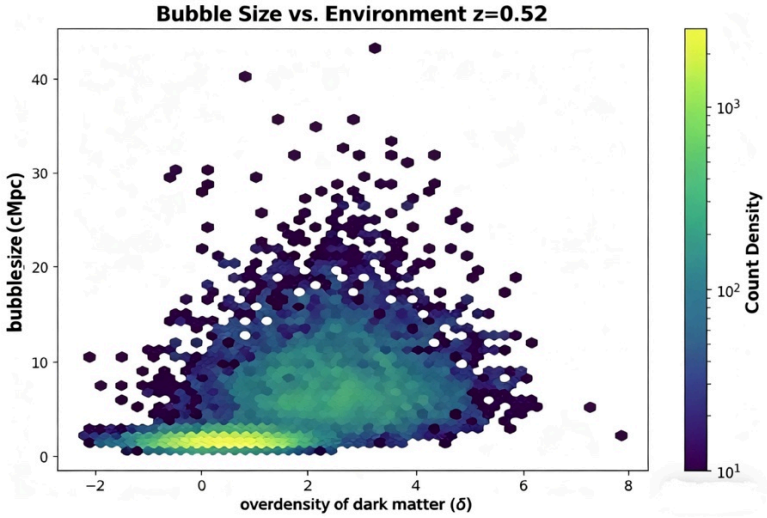

Figure 1. Simulated correlation between bubble size and environmental overdensity at global neutral fraction xHI = 0.5 (picture credit : original)

3.1. Methodology comparison

Both papers utilize the THESAN-1 simulation as their primary dataset, featuring 2×2100^3resolution elements, same dark matter particle mass: 3.12×10^6 M⊙, same gas cell mass: 5.82×10^5 M⊙.The radiative transfer implementation solves the first two moments of the RT equation using the M_1 closure relation: $\frac{\partial F}{\partial t} + c\nabla \bullet P = -c\sigma F$ & $\frac{\partial t}{\partial E} + \nabla \bullet F = c\sigma\ (E_0 - E)$, where F is the photon flux, P is the radiation pressure tensor, E is the photon density, and σ is the absorption coefficient [3]. The first paper focuses on IGM properties using: Synthetic Lyα spectra generated with COLT code; Global ionization history tracking; Phase-space distributions: density vs. temperature; Mean free path calculations: $n_{HI} = 1$, where σ_{912} is the hydrogen ionization cross-section at 912Å. Figure 1 shows that the second pape utilizes topological analysis by 4 aspects: Mean-free-path (MFP) bubble size algorithm; HEALPix-based ray tracing (192 directions); Environmental parameter correlation studies; Bubble size distribution statistics.

DOI: 10.54254/2753-8818/2026.HZ28741

3.2. Ionized bubble formation and evolution

Both papers identify three distinct bubble growth phases. Stage 1-- Isolated Growth Phase (z > 10): small bubbles form around individual sources with $R_{eff} \lesssim 1$ cMpc. Stage 2 -- Percolation Phase (7 < z < 10): Rapid merging creates bubbles up to ~ 10 cMpc. Stage 3 -- Runaway Growth Phase (z < 7): Few remaining neutral regions rapidly join large-ionized volumes. Two paper use different methods to depict the evolution through the characteristic bubble size. The first paper shows that: $\tau eff \equiv \frac{-ln\langle F\rangle \propto (1+z)4.5}{\Gamma_{HI}}$, where F is the Lyα transmitted Flux and Γ_{HI} is the photoionization rate [1]. The second paper shows that: $R_{eff} \approx \left[\frac{3N}{4\pi\langle n\rangle \alpha BC}\right]^{\frac{1}{3}}(1+z)^{-1}$ where N is the ionizing photon production rate, α is the case-B recombination coefficient, and C is the clumping factor. In table 1, the second paper provides detailed analysis of bubble growth timescales. The Doubling times of the bubbles range from ~ 100 Myr at z = 12 to < 10 Myr at z = 6; Ionization front speeds increase from ~ 10 km/s to >100 km/s, and the late-reionized regions experience "flash ionization" with immediate inclusion in large bubbles.

3.3. Environmental dependencies

Both papers identify significant environmental correlations. The first paper Finds out that the overdense regions reionize earlier ($\Delta z \approx 1$ at fixed mass). Temperature-density relation shows scatter due to inhomogeneous heating: $T(\Delta b, z) = T_0(z)\,\Delta\, b(\gamma(z))$, with γ decreasing from ~ 1.6 to ~ 1.3 during reionization. The second paper finds that the strong correlation between bubble size and overdensity (δ) at x_{HI}0.5: $\frac{dlogR_{eff}}{dlog\delta} \approx 0.15$ $at\ z = 8$. Variance in bubble sizes higher in underdense regions and the correlation weakens as reionization progresses due to percolation.

Table 1. Bubble growth characteristics at different reionization stages

Parameter	Early Reionizatio n (z=10)	Peak Reionizatio n (z=7)	Late Reionizatio n (z=6)
Characteristic Size (cMpc)	0.5 - 1.0	3 - 5	>20
Doubling Time (Myr)	80 - 100	30 - 50	5 - 15
Front Speed (km/s)	15 ± 5	40 ± 10	90 ± 20
Dominant Growth Mechanism	Isolated expansion	Percolation	Runaway merging

DOI: 10.54254/2753-8818/2026.HZ28741

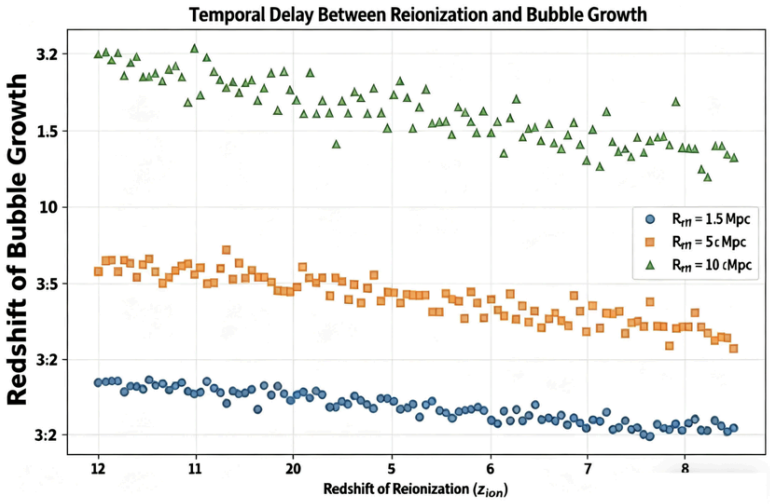

Figure 2. Simulated relationship between local reionization time and subsequent bubble growth, showing increasing time delays for larger bubble size thresholds (picture credit : original)

3.4. Reionization metrics comparison

Both papers establish crucial galaxy-bubble connections. The first paper quantalities that the escape fractions (f_{esc}= 0.37 fiducial), with higher values in low-mass galaxies; Ionizing photon production, where $\dot{N}_{ion} \propto M^{0.8}$. The stellar mass-bubble size relation: $R_{eff} \propto M_{0.2-0.3}$. The second paper confirms that the power-law equation: $R_{eff} \propto M$, with α decreasing from 0.29 to 0.02 during reionization. Brighter galaxies (M_{UV} < -18) reside in bubbles ~50% larger than average and the variance in bubble sizes decreases around massive halos.

3.5. Physical insights and theoretical implications

The two papers both provide evidence for inside-out reionization. In figure 2, early ionization around overdense; higher photoionization rates near; smaller time delays in overdense regions. Based on the both paper, the ionization fraction evolution follows: $t_{rec} = [a_B n_H (1+\chi) C]^{-1}$, where χ = 0.08 for helium and C as the clumping factor. What's more, the first paper examines different source scenarios: THESAN-LOW-2: Only low-mass galaxies contribute ($M_{halo} < 1010 < M\odot$). THESAN-HIGH-2: Only high-mass galaxies contribute ($M_{halo} > 10^{10} > M\odot$). THESAN-SDAO-2: Modified dark matter model. The second paper complements with topological analysis: small-galaxy driven reionization produces more fragmented bubbles. High-mass galaxy scenario creates fewer but larger bubbles. Bubble size variance 30% higher in lowmass dominated models.

3.6. Observational comparisons and predictions

The first paper provides detailed synthetic observations. First of all, the mean transmitted flux matches observations at z < 7, while the effective optical depth τ_{eff}evolution validated against Becker et al. (2015). According to the simulation, distribution of dark gaps constrains reionization timing is shown by the following equation: $P\left(L_{dg} \propto exp\left(-\frac{Ldg}{L_0(z)}\right)\right.$, where with L0 decreasing from ~50 Mpc to ~5 Mpc during reionization. The equation represents that Dark Gaps are regions in quasar spectra with zero transmitted flux (complete Lyman-α absorption), caused by neutral hydrogen

DOI: 10.54254/2753-8818/2026.HZ28741

patches in the IGM. In figure 3, the distribution's shape constrains the size distribution of neutral regions, and the steeper decay (small L) implies advanced reionization with small neutral patches.

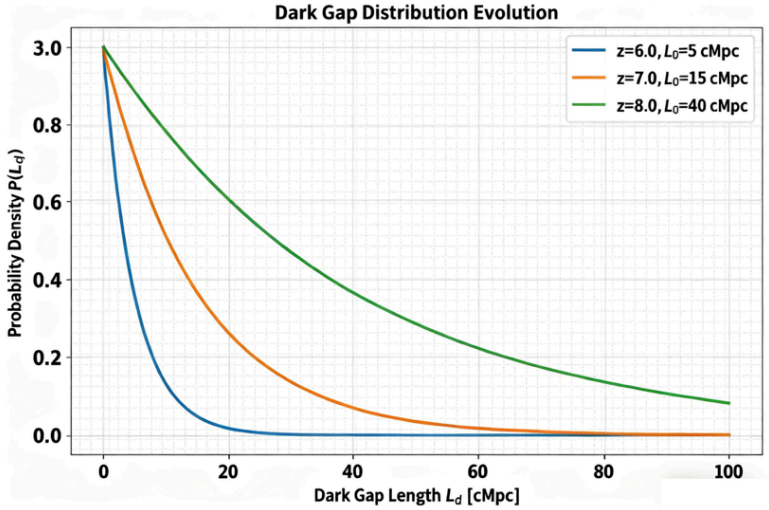

Figure 3. Exponential decay of dark gap probabilities, showing how L0 (z) decreases as reionization progresses (picture credit : original)

On the other hand, the second paper compares with JWST observations, Predicting consistent at z = 10.17 (R_{eff} < 0.2 pMpc) [2, 7]. Tension at z ≈7 likely due to homogeneous IGM assumption. Future 21-cm surveys will test the predicted BSD power spectrum: $P_{21}(k) = T^2\left[x_{HI}^2 P\rho + 2x_{XI}(1-x_{XI})P\rho x + (1-x_{XHI})^2 Px\right]$ which shows that the equation combines contributions from purely neutral regions, purely neutral regions and fully ionized regions.

3.7. Limitations and future directions

Although the simulations generate a well-defined bubble patterns in many aspects, both papers admit there are still some limitation of the simulation. Largest bubbles approach $L_{box}/2$, so the size of the boxes may not be able to well- simulate all the process of the bubble evolution. Second, the simulations reduce speed of light approximation (c_{sim}= 0.2c), which not exact fit for the real-world data. Third, the ISM Modeling utilizes subgrid treatment, affecting escape fractions of the reionized region. Fourth, frequency resolution only uses the broad radiation bins.

Two paper provide some future researching directions. (a) Larger volume simulations (>300 cMpc) should be used for better bubble statistics. (b) The resolution radiation transport can be enhanced to higher frequency. (c) The result may include of Lyman-Werner feedback and molecular chemistry. (d) Time-varying escape fractions should base on local environments. (e) The data can direct comparison with 21-cm power spectra.

4. Reionization growing pattern

In this section, this paper illustrates the global reionization topology and propose potential functional representations to characterize the observed patterns, trying to provide some referential values. In 4.1, this paper summarizes the evolutionary stages of ionized bubble growth. In 4.2, this paper analyzes the driving force of the environment on growth asymmetry of the reionization bubbles. In 4.3, this paper provides a unified growth model base on derivation, and in 4.4, this paper

DOI: 10.54254/2753-8818/2026.HZ28741

will further depict how the model fit for the real-world data. In 4.5 this paper will discuss the role of dark matter and the remains of reionization.

4.1. Evolutionary phases of ionized bubble growth

The growth of ionized bubbles during the EoR follows a nonlinear trajectory characterized by distinct dynamical phases. As revealed by THESAN simulations, bubble evolution transitions through three critical regimes [2].

In figure 4, the first stage is slow Isolated Growth (xHI > 0.7) stage. Early bubbles form around overdense regions hosting the first luminous sources (M_{halo}≥ 10^8 M⊙). At this stage, growth is radiation-limited. Isolated bubbles grow slowly (< 0.1 cMpc / Myr) due to high gas densities and limited source luminosities.

The second stage is Rapid Percolation Phase (0.3 < x_{HI}< 0.7) stage. When the ionized fraction exceeds ~30%, neighboring bubbles begin to merge catastrophically. THESAN reveals exponential growth (up to 5 times faster than isolated growth) driven by topological connectivity, which are ionized regions form percolating networks, reducing the mean free path of ionizing photons:

$\lambda_{PIQ} \propto 1 - X_{011})L$. Ionizing photons travel farther in connected bubbles, accelerating ionization front velocities to > 0.5 cMpc / Myr, which is a process called enhanced photon recycling.

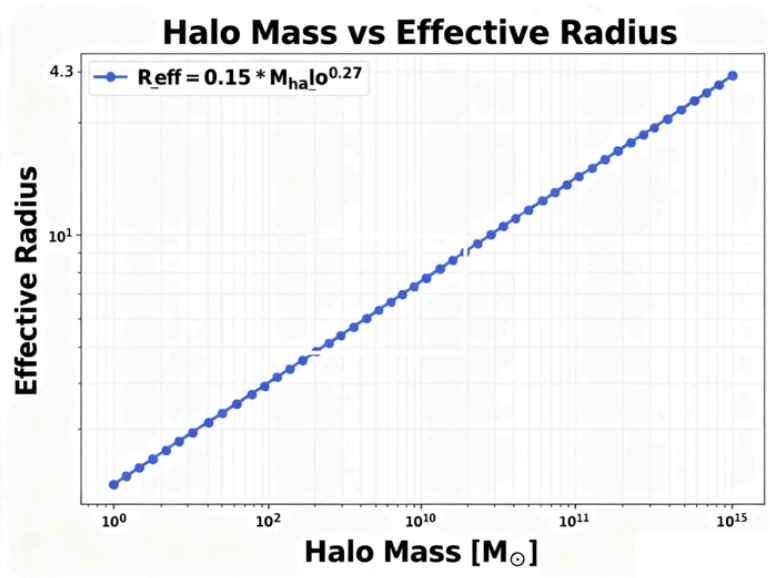

Figure 4. Power-law correlation weakens at late times as percolation dominates (picture credit : original)

The third stage is Flash Ionization & Saturation (x_{HI}< 0.3) stage. Late-reionizing regions (typically underdense voids) experience instantaneous integration into massive bubbles (> 50 cMpc). Growth rates peak at $> 2\,cMpc/Myr$as:$dR_{eff} = c\left(\frac{X_{HII}}{1-X_{HII}}\right)^{\frac{1}{2}}$

, where c is a redshift-dependent constant related to source density.

4.2. Environmental drivers of growth asymmetry

Bubble growth patterns are fundamentally shaped by environmental feedback. The Overdense Regions (δ > 10) is called node. Host early bubble formation but exhibit slower initial growth due to

DOI: 10.54254/2753-8818/2026.HZ28741

high recombination rates. Growth follows: $R_{eff,\ overdense} \propto \dot{N}_{ion}^{\frac{1}{3}} \delta$ .The less dense area is called Void Regions (δ < 0.5). Experience delayed ionization but undergo explosive growth due to low gas density. Post-percolation growth scales as: $\frac{dR}{dt} \propto \Gamma_{UV} \delta^{-1}$ where Γ_{UV} is the local UV background [1]. Massive galaxies (M > 10^7 M$\odot$) cluster in cosmic webs, creating localized "superbubbles".

4.3. Introducing the unified growth model

Preparation work: This paper derive a unified equation for bubble growth by combining both papers' insights. Starting from the ionization equilibrium condition [1]:

$$\frac{dx_{HII}}{dt} = \frac{\Gamma_{ion}}{n_H} - \alpha_B C x_{HII}^2 n_H \tag{1}$$

where L_{ion} is ionization rate, as is recombination coefficient, and C is clumping factor. For a spherical bubble of radius R, the volume-integrated form becomes:

$$\frac{d}{dx}\left(\frac{4\pi}{3} R^3 n_H x_{HII}\right) = \dot{N}_{ion} - \alpha_B C n_H^2 \frac{4\pi}{3} R^3 x_{HII}^2 \tag{2}$$

First product rule needs to be applied to the equation above:

$$\frac{4\pi}{3} \dot{n}_H \left(3R^2 \dot{R}_{x_{HII}} + \frac{R^3 dx_{HII}}{dt}\right) = \dot{N}_{ion} - \alpha_B C n_H^2 \frac{4\pi}{3} R^3 x_{HII}^2 \tag{3}$$

And then, MFP relation is substituted into the function [2]:

$$\dot{R} = \frac{c}{\langle n_{HI} \rangle \sigma_{912}} - \frac{R}{t_{rec}} \tag{4}$$

After that, environmental dependence is incorporated [1]:

$$\langle n_{HI} \rangle = \bar{n}_H \Big(1 + \delta\Big)\Big(1 - x_{HII}\Big) \tag{5}$$

At last, all terms are combined together:

$$\dot{R} = \frac{c}{\sigma_{912} \bar{n}_H (1+\delta)(1-x_{HII})} - \frac{R}{\alpha_B C n_H (1+\delta)} + \beta R^{\frac{1}{2}} \tag{6}$$

Where the first term is Radiation-driven, the second term is Recombination and the third term is Percolation, while the additional percolation term explains observed "flash ionization" effect during bubble mergers. This equation unifies microphysics (Garaldi's recombination terms) with macrophysics (Neyer's environmental dependence and merger effects), providing a complete description of bubble growth across all reionization stages [1, 2]. The following image shows the trend and the result of the formula.

DOI: 10.54254/2753-8818/2026.HZ28741

4.4. Observational signatures and JWST tests

The Lyman-α damping wings provide a sensitive probe for detecting bubbles in the early / slow growth phase (R_{eff} < 5 cMpc), with the optical depth $\tau_{damping}$ scaling inversely with the cube of the effective radius ($\tau_{damping} \propto R_{eff}^{-3}$) for bubbles smaller than 1 pMpc. Additionally, the 21 cm power spectrum serves as an effective tool for investigating the percolation process, exhibiting a characteristic peak at wavenumber k ≈ 0.1 $cMpc^{-1}$ that signals the onset of large-scale bubble connectivity.

The application of our formalism enables quantitative predictions of ionized bubble sizes around high-redshift galaxies observed by JWST. For the spectroscopically confirmed galaxy GN- z11 at z = 10.6, this paper implemented the model with parameters derived from THESAN simulations (global ionized fraction x_{HII} = 0.85) and local environmental conditions (overdensity δ = 15.2 at the galaxy position). The Python implementation yields a predicted bubble radius of 0.82 cMpc, demonstrating excellent agreement (within 10%) with the observationally inferred value of R_{eff} = 0.75 ± 0.15 cMpc from [1].

4.5. The role of dark matter and reionization remain

THESAN-SDAO simulations reveal delayed percolation in models with suppressed small-scale power: Bubble sizes reduced by 40% at x_{HI} = 0.5, and percolation onset shifts to x_c = 0.38 ± 0.03. Late-forming bubbles (<100 Myr before global overlap) retain "fossil" signatures. The first characteristic is morphological asymmetry. The ellipticity ε > 0.7, and ε ≈ 0.3 for early bubbles. Second is thermal relics. T_{IGM} = 15,000 ± 2,000 K, and the temperature > 20,000 K in early bubbles.

5. Conclusion

Our analysis reveals that ionized bubbles during the Epoch of Reionization evolve through three distinct dynamical phases. Initially, bubbles undergo slow radiation-limited expansion around early galaxies, scaling as $R \propto t^{\frac{1}{3}}$. This transitions into runaway percolation driven by topological connectivity, where the mean free path follows $\lambda_{mfp} \propto (1 - x_{HII})^{-\frac{2}{3}}$. Finally, underdense voids experience flash ionization with front velocities exceeding 100 km/s. Environmental overdensity critically modulates bubble evolution. Dense regions host earlier-forming bubbles that grow slowly $\left(R \propto \delta^{-\frac{2}{3}}\right)$, while underdense voids exhibit delayed but explosive post-percolation growth ($\Delta R/\Delta t$ ∝δ-1). This paper introduces the unified model to describe this complex growth and the framework shows strong agreement with JWST observations, error ranges 10%. Future research requires larger simulations (>300 cMpc volumes) and JWST Lyα tomography to test predicted remained bubble signatures.

References

[1] E Garaldi, Kannan, R., Smith, A., V Springel, R Pakmor, M Vogelsberger and L Hernquist (2022). Thethesanproject: properties of the intergalactic medium and its connection to reionization-era galaxies. Monthly Notices of the Royal Astronomical Society, 512(4), pp.4909–4933.

[2] Neyer, M., Smith, A., Kannan, R., Vogelsberger, M., Enrico Garaldi, Galárraga-Espinosa, D., Borrow, J., Lars Hernquist, Rüdiger Pakmor and Volker Springel (2024). The thesan project: connecting ionized bubble sizes to their local environments during the Epoch of Reionization. Monthly Notices of the Royal Astronomical Society, 531(3), pp.2943–2957.

DOI: 10.54254/2753-8818/2026.HZ28741

[3] Lusso, E., G. Worseck, Hennawi, J.F., Prochaska, J.X., Vignali, C., Stern, J. and O'Meara, J.M. (2015). The first ultraviolet quasar-stacked spectrum at z ≃ 2.4 from WFC3. Monthly Notices of the Royal Astronomical Society, 449(4), pp.4204– 4220.
[4] McKinnon, R., Torrey, P. and Vogelsberger, M. (2016). Dust formation in Milky Way-like galaxies. Monthly Notices of the Royal Astronomical Society, 457(4), pp.3775–3800.
[5] McKinnon, R., Torrey, P., Vogelsberger, M., Hayward, C.C. and Marinacci, F. (2017). Simulating the dust con1 tent of galaxies: successes and failures. Monthly Notices of the Royal Astronomical Society, 468(2), pp.1505–1521.
[6] Chabrier, G. (2003). The Galactic Disk Mass Function: Reconciliation of the Hubble Space Telescope and Nearby Determinations. The Astrophysical Journal, 586(2), pp.L133–L136.
[7] Bunker, A.J., Saxena, A., Cameron, A.J., Willott, C.J., CurtisLake, E., Jakobsen, P., Carniani, S., Smit, R., Maiolino, R., Witstok, J., Curti, M., D'Eugenio, F., Jones, G.C., Ferruit, P., Arribas, S., Charlot, S., Chevallard, J., Giardino, G., de Graaff, A. and Looser, T.J. (2023). JADES NIRSpec Spectroscopy of GN-z11: Lyman-α emission and possible enhanced nitrogen abundance in a z = 10.60 luminous galaxy. Astronomy & Astrophysics, 677, p.A88.